$\mathcal{PT}$-symmetric Helmholtz resonator dipoles for sound directivity

Tetsu Magariyachi [*,†]

Sony Corporation, 1-7-1 Konan, Minato-ku, Tokyo, 108-0075, Japan

Helena Arias Casals, Ramon Herrero, and Muriel Botey

Departament de Física, Universitat Politècnica de Catalunya, Colom 11, E-08222 Terrassa, Barcelona, Spain

Kestutis Staliunas [†]

Institució Catalana de Recerca i Estudis Avançats, Passeig Lluís Companys 23, E-08010, Barcelona, Spain

Parity-time ($\mathcal{PT}$)-symmetric or, more generally, non-Hermitian systems have opened a new area for unconventional management of waves, with significant applications, especially in optics. However, fewer proposals are found in acoustics, possibly due to the lack of a simple mechanism for coherent gain. In this paper, we propose a composite non-Hermitian system in acoustics consisting of assemblies of $\mathcal{PT}$-symmetric Helmholtz resonator (HR) dipoles. Like meta-atoms are used as building elements in metamaterials, we propose $\mathcal{PT}$-symmetric dipoles to design non-Hermitian systems intended to engineer complicated directivity fields. We theoretically analyze, numerically confirm, and experimentally show the symmetry breaking in a two-dimensional space of non-Hermitian dipoles consisting of a pair of Helmholtz resonators with different levels of gain and loss. In particular, we explore, as an application, a metastructure to concentrate the sound pressure inside the circular array formed by $\mathcal{PT}$-symmetric dipoles. The proposed HR dipoles may be a convenient composite element for smart control of sound.

I. INTRODUCTION

Non-Hermitian systems, in particular, those holding invariance under parity-time ($\mathcal{PT}$) inversion, have recently opened new horizons for the smart manipulation and control of classical waves, despite having been discovered in the frame of quantum mechanics [1]. Possibly, the most exceptional property of $\mathcal{PT}$-symmetric systems is the spontaneous breaking of the spatial symmetries at a $\mathcal{PT}$ symmetry-breaking point. In particular, an asymmetric response arises when the real and imaginary parts of the complex (non-Hermitian) potentials are related by the spatial Kramers-Kronig relations (Hilbert transform) [2,3]. Thus, such a space symmetry breaking occurs for potentials with specific spatial shifts between real and imaginary parts. The spatial modulation design of such potentials can be either discrete, based on localized oscillators, or continuous, based on a spatially distributed modulation of gain/loss (real part) and wave velocities (imaginary part). In one-dimensional systems, symmetry breaking manifests as the difference between the reflections from the right and left. Higher-dimension non-Hermitian systems allow not only uniform symmetry breaking and uniform directivity but also spatially dependent directivities, determined by a local (generalized) Hilbert transform [4,5]. This extends the possibilities of wave control to exotic effects such as wave localization or self-cloaking [6], among others.

Possibly, the most convenient and most explored playground for the observation of non-Hermitian effects is optics, where coherent gain arises from the stimulated emission of radiation, permitting a feasible design for non-Hermitian systems. Non-Hermitian systems, being either discrete (pointlike) with $\mathcal{PT}$-symmetric couplings [7,8] or continuous (with a spatially distributed bulk gain/loss), have been both theoretically considered [9–12] and experimentally demonstrated [13,14] and even applied for practical purposes [15]. Yet a collection of discrete elements may also be used to build a metamaterial, i.e., a continuous system where the individual elements and the distances between the individual elements are significantly smaller than the wavelength. Such is the main idea behind metamaterials for microwave electromagnetic resonators, where the role of the meta-atom is played by a resonant circuit or antenna [16–18]. Such metamaterials are passive due to the lack of compact amplification mechanisms in this wavelength range. However, they can show a negative refractive index and other striking directional properties such as unidirectional invisibility [6,19]. In acoustics, asymmetric absorption has been demonstrated by detuned Helmholtz resonators (HRs) in one-dimensional waveguides [20]. More recently, one- and two-dimensional arrays of HRs were designed to achieve efficient sound absorption and diffusion [21]. Accordingly, a spatial distribution of HRs with modulated resonant frequencies and gain/loss can be feasible acoustic metamaterials, analogous to those in optics and microwave ranges. There is no clear way to achieve acoustic amplification in continuous systems, and in fact, all $\mathcal{PT}$ symmetry effects in acoustics have been demonstrated on discrete systems using intricate gain/loss methods,

---

*Tetsu.Magariyachi@sony.com

†Also at Departament de Física, Universitat Politècnica de Catalunya, Colom 11, E-08222 Terrassa, Barcelona, Spain.
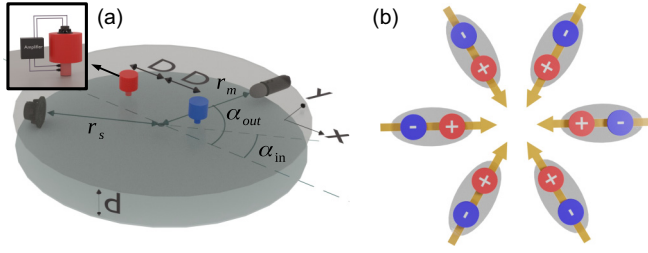
FIG. 1. (a) A HR dipole consisting of two HRs with amplification and attenuation, coupled to a planar waveguiding structure. The microphone-loudspeaker arrangement is illustrated in the inset. Such a dipole, as shown in the text, is expected to show directional scattering. The distances of the loudspeaker and the microphone to the center of the dipole are defined as r_s and r_m, respectively, and the incident and observation angles are defined as α_{in} and α_{out}, respectively. (b) An ensemble of $\mathcal{PT}$-symmetric dipoles with a specific arrangement to form the patterns of sound flows. In this particular example the dipoles are arranged to form a sink in the symmetry center.
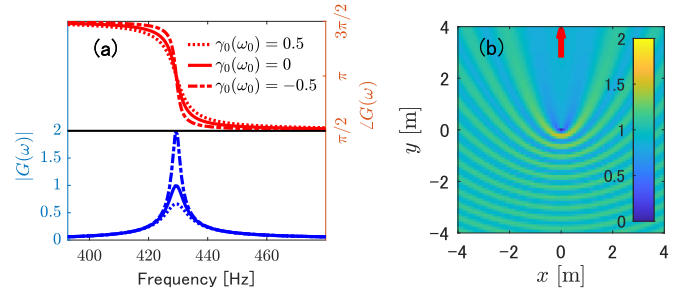

FIG. 2. (a) Frequency responses and gain function $G(\omega)$ of a single HR with (i) loss (dotted curve), (ii) neither loss nor active gain (neutral; solid curve), and (iii) gain (dashed curve). Negative (positive) loss factors $\gamma_0(\omega_0)$ correspond to active gain (active losses) generating peak amplitudes higher (lower) than 1 and sharper (smoother) phase shifts. (b) Total pressure field created by the incident plane wave and the scattered wave from a neutral HR at the origin. The source frequency is $f = 429.1$ Hz, corresponding to the peak of the gain functions. Fringes are observed around the HR, indicating the interference between the incident and scattered fields. The parameters were set as $a = 2$ mm, $d = 20$ mm, $l' = 13.07$ mm, $f_0 = 436.3$ Hz, and $c = 340$ m/s.

like a net of microphones and loudspeakers with electronic amplification/attenuation in between. However, many examples of $\mathcal{PT}$-symmetric systems without positive gain may exhibit the same expected effects, just with an additional homogeneous loss.

Possibly, the simplest method to construct $\mathcal{PT}$-symmetric lattices is the arrangement of individual $\mathcal{PT}$-symmetric dipoles ($\mathcal{PT}$ dipoles) showing asymmetric scattering [22]. The directivity at each spatial point will be given by the orientation of the $\mathcal{PT}$ dipoles at a particular location. Here, we propose ensembles of HR dipoles, each one consisting of an amplifying HR and an attenuating HR, to build active acoustic metamaterials. The benefit of using HRs as $\mathcal{PT}$-scattering elements stems from their high sensitivity to long wavelengths as compared to their size. This feature confers flexibility to the geometric configuration. The main body of this paper is devoted to the calculation and experimental demonstration of the radiation properties of $\mathcal{PT}$-symmetric HR dipoles as building blocks of complex non-Hermitian metastructures; see Fig. 1(a) for illustration. This is the minimum system to break the spatial symmetry in a non-Hermitian way and to demonstrate the control of sound.

The study is performed in a two-dimensional (2D) space, such as the minimal configuration to demonstrate the sound directivity arising from the asymmetric scattering, which is the main goal of the paper. In turn, different sophisticated sound manipulation effects may be expected from given $\mathcal{PT}$-dipole arrangements; for instance, Fig. 1(b) is intended to archive strong concentrations of sound, which have also been proposed in the field of transformation optics/acoustics [23–25]. The last part of the work proposes oriented $\mathcal{PT}$-symmetric HR dipole structures.

II. HELMHOLTZ RESONATOR DIPOLES IN 2D SPACE

A. Single Helmholtz resonator

We first introduce the governing equations of a Helmholtz resonator (HR) and briefly discuss the derivation of the HR gain function (the full derivation is provided in

Appendix A). We assume a HR placed at $\vec{r} = \vec{0}$, subjected to an input pressure field $P_{in}(\omega)$, emitting an isotropic pressure field $P_{scat}(\vec{r}) = H_0^{(2)}(kr) P_{out}(\omega)$, where $H_0^{(2)}(kr)$ denotes a Hankel function of the second kind. The gain function may be defined as

$$G(\omega) = \frac{P_{out}(\omega)}{P_{in}(\omega)}, \tag{1}$$

which for the considered geometry of the HR (see Appendix A) is expressed as

$$G(\omega) = \frac{1}{G_0^{-1}(\omega) - 1 - i\frac{2}{\pi}\ln\left(\frac{2}{\epsilon ka}\right)}, \tag{2}$$

where ω is the angular frequency, $k (= \omega/c)$ is the wave number, c is the sound velocity, a is the cross-section radius of the HR neck, and the parameter $\epsilon = 1.7812$;

$$G_0(\omega)^{-1} = i\gamma_{c2}^{-1}\left(\frac{\omega_0^2}{\omega^2} - 1\right) - \gamma_0(\omega) \tag{3}$$

where ω_0, γ_{c2}, and $\gamma_0(\omega)$ denote the resonant angular frequency of the HR, the coupling loss factor, and the relative loss factor of the HR in a two-dimensional space:

$$\gamma_{c2} = \frac{S_h}{4dl'}, \quad \gamma_0(\omega) = \frac{\gamma}{\gamma_{c2}\omega}, \tag{4}$$

where d is the thickness of the 2D field, l' is the corrected HR neck length, S_h is the cross section of the HR neck, and γ is the loss factor of the HR. Unless otherwise specifically noted, hereafter, we omit ω from G, P_{in}, and P_{out} for brevity.

Figure 2 depicts a numerical integration of the gain function [Eq. (2)]; it provides an example of the resonant curves for three different situations: (i) a HR with loss [$\gamma_0(\omega_0) = 0.5$], (ii) a neutral HR [$\gamma_0(\omega_0) = 0$ with neither active gain nor loss], and (iii) a HR with gain [$\gamma_0(\omega_0) = -0.5$]. In Fig. 2(a), we observe that the peak of the gain is 1 for a neutral HR

$[\gamma_0(\omega_0) = 0]$, becoming either smaller or larger for the cases with loss and active gain, respectively [for $\gamma_0(\omega_0) = 0.5$ and -0.5]. Further, the peak frequency ($f = 429.1$ Hz) is observed to be lower than the resonant frequency ($f_0 = 436.3$ Hz). This is a consequence of the coupling to the 2D field; indeed, it derives from the imaginary term inside the denominator of Eq. (2). Note that Eq. (2) has a sense for amplification when $\gamma_0(\omega) < 0$. In the case of large gain, $\gamma_0(\omega) \leqslant -1$, the HR starts "generating." The effect is similar to a pitch sound in a closed-circuit microphone-amplifier-loudspeaker when the microphone is placed too close to the loudspeaker. An example of the full field distributions from a plane wave exciting a neutral HR without loss [situation (i)], located at $\vec{r} = \vec{0}$, is shown in Fig. 2(b). The source frequency in this case is $f = 429.1$ Hz, precisely at the peak of the gain function. The pressure field is normalized by the absolute incident pressure. We can clearly observe fringes from the center to the surroundings except in the direction of the incident wave due to the interference of the incident field and field scattered by the HR.

B. Ensemble of Helmholtz resonators

Next, we consider the scattered field from a general ensemble of N HRs. We assume N different HRs with respective gain functions $G_1, \ldots, G_N$ located at a particular spatial position in a 2D space $\vec{r}_1, \ldots, \vec{r}_N$. The source is located at $\vec{r}_s$, while the pressure field scattered from all the HRs is observed at a position $\vec{r}_m$. In this case, instead of Eq. (2), the system is described by the system of equations

$$p_{in} = p_0 + H_0 p_{out},$$
$$p_{out} = G p_{in}, \tag{5}$$

with

$$p_0 = h_s(\vec{r}_s)P_0, \quad p_{in} = \begin{pmatrix} P_{in1} \\ \vdots \\ P_{inN} \end{pmatrix}, \quad p_{out} = \begin{pmatrix} P_{out1} \\ \vdots \\ P_{outN} \end{pmatrix},$$

$$h_s(\vec{r}_s) = \begin{pmatrix} H_0^{(2)}(k|\vec{r}_1 - \vec{r}_s|) \\ \vdots \\ H_0^{(2)}(k|\vec{r}_N - \vec{r}_s|) \end{pmatrix},$$

$$G = \begin{pmatrix} G_1 & 0 & \cdots & 0 \\ 0 & G_2 & \ddots & \vdots \\ \vdots & \ddots & \ddots & 0 \\ 0 & \cdots & 0 & G_N \end{pmatrix},$$

$$H_0 = \begin{pmatrix} 0 & H_{21} & \cdots & H_{N1} \\ H_{12} & 0 & \ddots & H_{N2} \\ \vdots & \ddots & \ddots & \vdots \\ H_{1N} & H_{2N} & \cdots & 0 \end{pmatrix},$$

$$H_{n_1 n_2} = H_0^{(2)}(k|\vec{r}_{n_2} - \vec{r}_{n_1}|),$$

where p_0, p_{in}, and p_{out} are the vectors of pressures at the positions of the HRs for the incident field, input field P_{in}, and scattered field P_{out}. The difference between p_0 and p_{in} is that the former includes only the pressure direct from the source

and the latter includes the pressure from the source and the scattered wave from other HRs (excluding the pressure from itself). Note that the fields at the entrance of each resonator depend on the fields at the output of each resonator plus the sound from the source. The system is solved by a matrix inversion:

$$p_{out} = (I - G H_0)^{-1} G p_0. \tag{6}$$

Also, when the interaction between the HRs is negligible, which is equivalent to satisfying the condition $\max\{G_1, G_2\}H_{12} \ll 1$, the first Born approximation holds, and we may assume

$$p_{out} \simeq G p_0. \tag{7}$$

Finally, the pressure at any arbitrary observation point $\vec{r}_m$ may be obtained as

$$P_{scat}(\vec{r}_s, \vec{r}_m) = h_m(\vec{r}_m)^T \tilde{G} h_s(\vec{r}_s)P_0, \tag{8}$$

with

$$h_m(\vec{r}_m) = \begin{pmatrix} H_0^{(2)}(k|\vec{r}_m - \vec{r}_1|) \\ \vdots \\ H_0^{(2)}(k|\vec{r}_m - \vec{r}_N|) \end{pmatrix},$$

$$\tilde{G} = (I - G H_0)^{-1} G.$$

In the following section we consider a HR's dipole; hence, $N = 2$.

C. Helmholtz resonator dipole

We propose a non-Hermitian dipole as the building block for sound directivity formed by two geometrically identical HR that are the same as the previous example in Fig. 2, but with different loss factors [$\gamma_0(\omega_0) = \pm 0.9$]. We here explore the asymmetric response of the HR dipole, whose results are summarized in Figs. 3 and 4. Both HRs are assumed to be at the positions $(x, y) = (\pm D, 0)$, i.e., placed at a distance of $|\vec{r}_1 - \vec{r}_2| = 2D$. In this case, we consider the source and observation points, namely, r_s and r_m, located far enough ($r_m > 4D^2/\lambda$) to allow assuming plane waves for both the incident and scattered waves. The response of the system is evaluated by scanning both $\vec{r}_s$ and $\vec{r}_m$ in $360°$. The results are mapped in Fig. 3. We want to note that the concept of directivity of the dipole is different from the directivity of an antenna. For antennas, the directivity diagrams are commonly plotted in polar coordinates, which fully characterize the antenna (for a given frequency). For the scattering of the HR dipole, the angular radiation diagram should be calculated for each incidence angle. Figure 3 summarizes this study, showing polar directionality diagrams for several incidence angles for a particular frequency of the source [see Figs. 3(b)–3(f)]. These diagrams are vertical cross sections from the full 2D multistatic matrix [26] $\bar{G}(\alpha_{in}, \alpha_{out})$ depicted in Fig. 3(a). Here, the multistatic matrix is calculated as

$$\bar{G}(\alpha_{in}, \alpha_{out}) = \frac{P_{scat}(\vec{r}_s, \vec{r}_m)}{P_0 H_0^{(2)}(k|\vec{r}_s|) H_0^{(2)}(k|\vec{r}_m|)}. \tag{9}$$

Throughout this paper, the incident angle α_{in} is defined as the angle of the incident wave vector towards the origin, which is
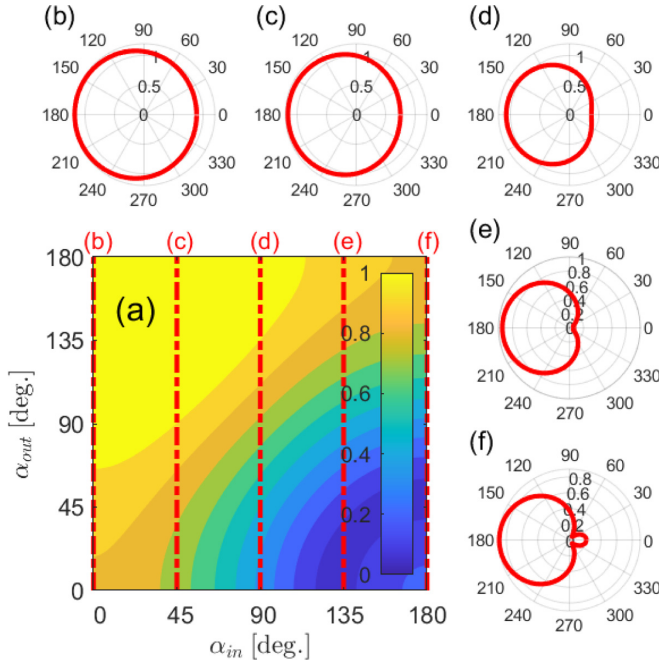
FIG. 3. (a) Multistatic matrix, i.e., the dependence of scattering on incidence angle α_{in} and observation angle α_{out}. The source frequency is $f = 432$ Hz, $D = 0.05$ m, $r_s = r_m = 100$ m, and the rest of the parameters are the same as in Fig. 2. (b)–(f) Polar plots of directivity for several incidence angles (which are the vertical cross sections of the map). Note that due to symmetries only 1/4 of the map is plotted (other quadrants can be obtained by mirror symmetries).
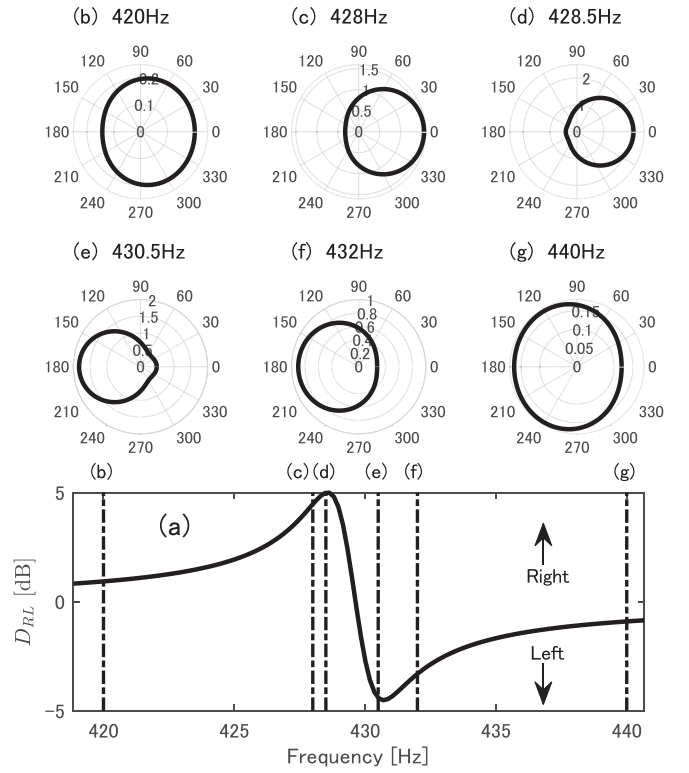

FIG. 4. Integrated directivity depending on frequency. (a) Intensity deflection in decibels as a function of frequency. (b)–(g) Integrated directivity in polar coordinates for several frequencies corresponding to the vertical dashed lines in (a).

therefore $180°$ opposite $\vec{r}_s$, while the observation angle α_{out} directly corresponds to the angle of $\vec{r}_m$ pointing in the direction where the pressure is measured. Because of the symmetry of the system's geometry about the x axis, Fig. 3(a) illustrates only the angular region of $0 \leqslant \alpha_{\text{in}} \leqslant 180°$ and $0 \leqslant \alpha_{\text{out}} \leqslant 180°$. We clearly observe a symmetry about the diagonal line ($\alpha_{\text{in}} + \alpha_{\text{out}} = 180°$), which is due to both the symmetry of the geometry about the x axis and the reciprocality. In contrast, we observe significant asymmetry about the other diagonal line ($\alpha_{\text{in}} = \alpha_{\text{out}}$), as expected from the symmetry breaking of the $\mathcal{PT}$-symmetric dipole. This tendency can also be observed from Figs. 3(b)–3(f). While the scattering shape is close to omnidirectional for Fig. 3(b), the directivity becomes gradually higher to the left as α_{in} increases and moves towards Fig. 3(f). Note that this result is strongly frequency dependent and that the map provided here is calculated at a frequency close to the dipole exceptional point.

To characterize the scattering properties of the dipole and to assess the $\mathcal{PT}$ symmetry-breaking effect, we integrate the scattering function $\tilde{G}$ over all incidence angles α_{in}. The integrated directivity (ID), indicating the overall scattering performance of the dipole, for a given frequency, is defined as

$$\text{ID}(\alpha_{\text{out}}) = \frac{1}{2\pi} \int_0^{2\pi} |\bar{G}(\alpha_{\text{in}}, \alpha_{\text{out}})|^2 d\alpha_{\text{in}}. \quad (10)$$

In this case the ID diagram, shown in Figs. 4(b)–4(g), is similar to that typically plotted in antenna theory. Finally,

we may obtain an asymmetry figure of merit evaluating the deflection ID with respect to the y axis $D_{\text{RL}}(f)$, i.e., the right to left directivity for a given frequency, as

$$D_{\text{RL}}(f) = 10 \ln \left(\frac{\text{ID}_R(f)}{\text{ID}_L(f)} \right), \quad (11)$$

with

$$\text{ID}_L = \frac{1}{\pi} \int_{\pi/2}^{3\pi/2} \text{ID}(\alpha_{\text{out}}) d\alpha_{\text{out}}, \quad (12)$$

$$\text{ID}_R = \frac{1}{\pi} \int_{-\pi/2}^{\pi/2} \text{ID}(\alpha_{\text{out}}) d\alpha_{\text{out}}. \quad (13)$$

This measure, illustrated in Fig. 4(a), reveals the intensity deflection to either side: left ($x < 0$) or right ($x > 0$), arising from the $\mathcal{PT}$ symmetry breaking, as a function of frequency.

In Fig. 4(a), it can be observed that the deflection to the right gradually becomes stronger, as the system shows unidirectional wave transport, and flips, for frequencies higher than the one corresponding to the peak of the gain function $|G(\omega)|$, to a strong deflection to the left. At exactly this transition point, the phase of $G(\omega)$ shifts from $3\pi/2$ to $\pi/2$ (see Fig. 2). Then, as the frequency increases, after the maximum deflection to the left, deflection becomes gradually weaker. Indeed, far from the resonance, we observe a weak deflection to right and left sides [see Figs. 4(b) and 4(g)], corresponding to particular frequencies in Fig. 4(a). In contrast, Figs. 4(c)–4(f) evidence a stronger deflection, either to the right [Figs. 4(c) and 4(d)] or to the left side [Figs. 4(e) and 4(f)]. It is worth

noticing that in Figs. 4(c)–4(f) the scattered intensity is almost four times higher in either direction at the angles 0° and 180°. As observed in Fig. 4, asymmetric effects appear precisely around the peak of the gain function $|G(\omega)|$ on both sides, left and right, depending on the frequency. This deflection tendency can be explained by the two-dimensional Fourier transform of the theoretical gain functions $G(x, y)$, as detailed in Appendix B. A comprehensive comparison of the Ewald limiting disk, in the wave vector domain, obtained both from the theoretical model and by direct numerical integration finds good agreement. In turn, such numerical calculations show the validity of the analytical model used to obtain the results of the multistatic matrix of the dipole (Fig. 3) and those of the ID in Fig. 4.

III. EXPERIMENTAL EVALUATION

To confirm the theoretical analysis of the scattering properties of the non-Hermitian HR dipole, we conducted an experiment using two HRs, both having the same geometric features, but with one having loss and the other one being neutral, with neither loss nor gain.

Figures 5(a) and 5(b) depict the full experimental setup and schematic transverse cut showing the specific geometric parameters, respectively. Prior to the experiment, we conducted a preexperiment using a one-dimensional (1D) waveguide, which is detailed in Appendix C. Besides representing an initial proof of the expected asymmetric left/right scattering of the non-Hermitian HR dipole, the preexperiment allowed experimentally determining some of the parameters of the HRs, which we directly used for the theoretical analysis in this 2D experiment. The loudspeaker was set at different angular positions α_{in} every 30° on a half circle from $\alpha_{\mathrm{in}} = 0°$ to 180° with radius $r_s = 130$ mm, while, in turn, the microphone was also set every 30° on the other half circle, i.e., from $\alpha_{\mathrm{out}} = 0°$ to 180°, on a circle with a radius of $r_m = 110$ mm. For every combination of microphone and speaker angles, first, we measure an impulse response (IR) without HRs and get a transfer function (TF), $P_0(\alpha_{\mathrm{in}}, \alpha_{\mathrm{out}})$. Then, we put a HR with no loss (HR1) at $(x, y) = (-D, 0)$ and the other HR with loss (HR2) at $(x, y) = (D, 0)$ and measured an IR to get the TF $P(\alpha_{\mathrm{in}}, \alpha_{\mathrm{out}})$. Next, the multistatic matrix $\bar{G}(\alpha_{\mathrm{in}}, \alpha_{\mathrm{out}})$ is calculated as

$$\bar{G}(\alpha_{\mathrm{in}}, \alpha_{\mathrm{out}}) = \frac{P(\alpha_{\mathrm{in}}, \alpha_{\mathrm{out}}) - P_0(\alpha_{\mathrm{in}}, \alpha_{\mathrm{out}})}{H_0^{(2)}(kr_m)\bar{P}_0}, \quad (14)$$

with

$$\bar{P}_0 = \frac{1}{7} \sum_{n=0}^{6} \frac{P_0\left(\frac{\pi n}{6}, \frac{\pi n}{6}\right) H_0^{(2)}(kr_s)}{H_0^{(2)}[k(r_s + r_m)]}. \quad (15)$$

Finally, on the grounds of the raw reciprocity, we averaged the matrix with itself flipped along the symmetric axis, $\alpha_{\mathrm{in}} + \alpha_{\mathrm{out}} = 180°$.

We show the results of the experiment in Figs. 5(c)–5(g), also providing a comparison with the theoretical calculation. Figure 5(c) illustrates the deflection $D_{\mathrm{RL}}(f)$, where the black solid and red dashed lines represent the theoretical and experimental data, respectively. It is clearly observed that the
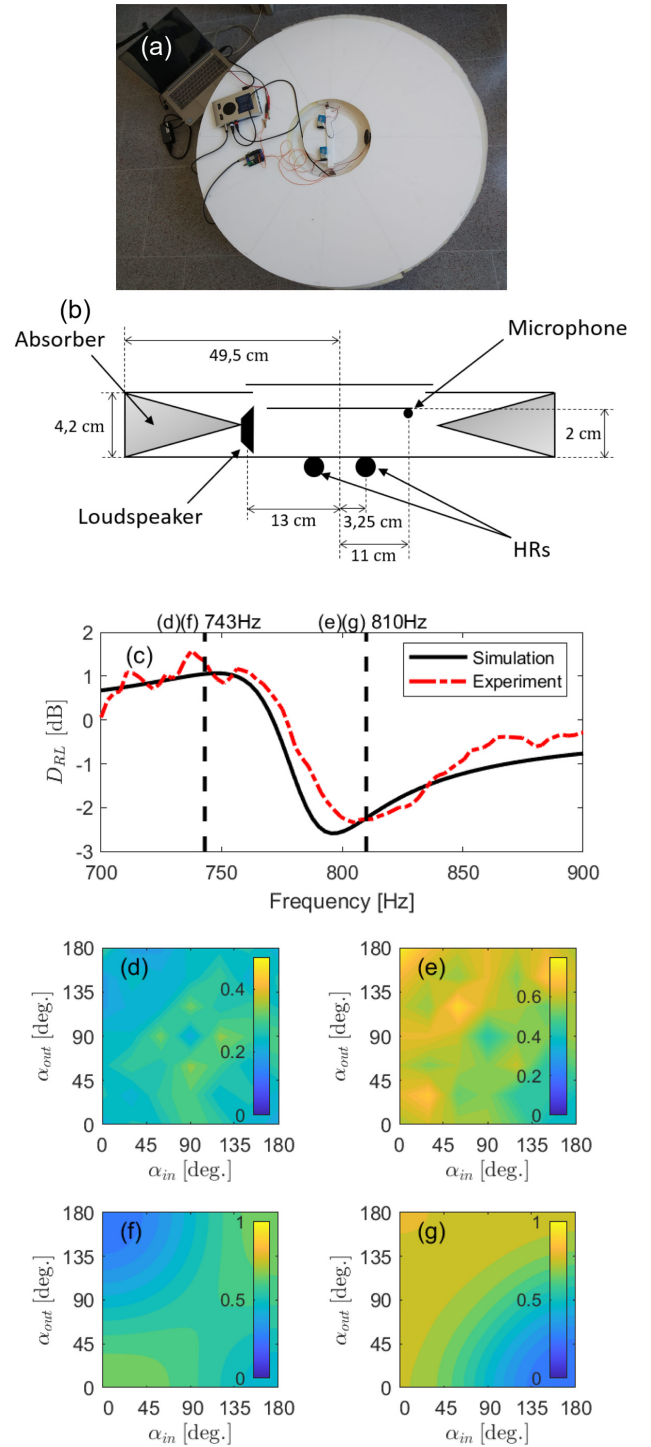

FIG. 5. Experimental setup and the result. (a) A picture of the experimental setup. (b) Geometry configuration of the setup with the viewpoint of the cross section. The parameters are set as $a = 5$ mm, $d = 20$ mm, $D = 32.5$ mm, $f_0 = 820$ Hz, $l' = 17.21$ mm, $r_m = 110$ mm, $r_s = 130$ mm, $\gamma_1/\gamma_{c1} = 0$, and $\gamma_2/\gamma_{c1} = 0.7$. See Appendix C. (c) Deflection analysis of the experimental result compared with the theoretical calculation. (d) and (e) Multistatic matrices of the experimental result for frequencies of 743 and 810 Hz, respectively. (f) and (g) Multistatic matrices of the theoretical calculation for the same frequencies as in (d) and (e).

experimental result has good agreement with the theoretical one. Both have a slight deflection to the right for the frequency region below 775 Hz. Then, a larger deflection to the left is observed as the frequency approaches 800 Hz, although the theoretical data have a peak around -2.5 dB at around 790 Hz and the experimental data have a peak around -2 dB at 800 Hz. We note that the theoretical results displayed for comparison are obtained with no fitting parameter expect those determined in the 1D preexperiment. Figures 5(d)–5(g) illustrate the multistatic matrices; Figs. 5(d) and 5(e) correspond to experimental results, and Figs. 5(f) and 5(g) correspond to the theoretical analysis for two particular frequencies: 743 Hz [Figs. 5(d) and 5(f)] and 810 Hz [Figs. 5(e) and 5(g)]. In Figs. 5(d) and 5(f), we clearly observe that both maps have the same tendency, having a large dip in the top left and a small dip in the bottom right and a soft peak a bit below the diagonal line of $\alpha_{in} = \alpha_{out}$. Also the maps in Figs. 5(e) and 5(g) show an analogous tendency, a monotonous increase in the scattering from the bottom right to the top left. The expected directionality induced by the asymmetric scattering of a non-Hermitian HR dipole is therefore evidenced in this neutral/loss configuration and is hence expected to be even higher for a gain/loss $\mathcal{PT}$-symmetric case.

IV. ENSEMBLES OF DIPOLES

The HR dipoles, with the specific characteristics discussed in the previous section, can be used as building blocks of a more complex metastructure. As a particular example we may demonstrate a sound field concentrator. We propose a HR dipole ensemble using a distribution like the one schematized in Fig. 1(b). Such a configuration is expected to concentrate the sound arriving from outside into one spot. We assume 10 dipoles distributed in a circle of 0.7-m radius, as illustrated in Figs. 6(a) and 6(b), where the HRs with gain are placed on the inner side of the structure inside Fig. 6(a). For comparison, we also consider the case where the HR dipoles are reversed, as in Fig. 6(b). We calculated the generated sound field upon incidence of a plain wave at a particular angle. The pressure field is normalized to the incident wave pressure at the origin without HRs and squared to obtain a normalized intensity, as shown in Figs. 6(c) and 6(d), where the source frequency was set to $f = 430.5$ Hz, which has the maximum deflection to the left, as depicted in Fig. 4. The normalized intensity fields are then calculated for every incident direction (every 5°) and averaged over all the incident angles. The results are shown in Figs. 6(e) and 6(f). A significant concentration is clearly shown in Fig. 6(e), in contrast to Fig. 6(f), when the dipoles are reversed.

V. CONCLUSION

We proposed acoustic $\mathcal{PT}$-symmetric dipoles in two-dimensional sound pressure fields, formed by two geometrically identical HRs with different loss factors (ideally, one with loss and another one with gain properties), as building blocks for the management of sound. The frequency response $G(\omega)$ of one HR in the 2D field was derived, and the response of the HR dipole was obtained using the analyses of the multistatic matrix and integral directivity, showing the expected asymmetric scattering in two dimensions. In addition,
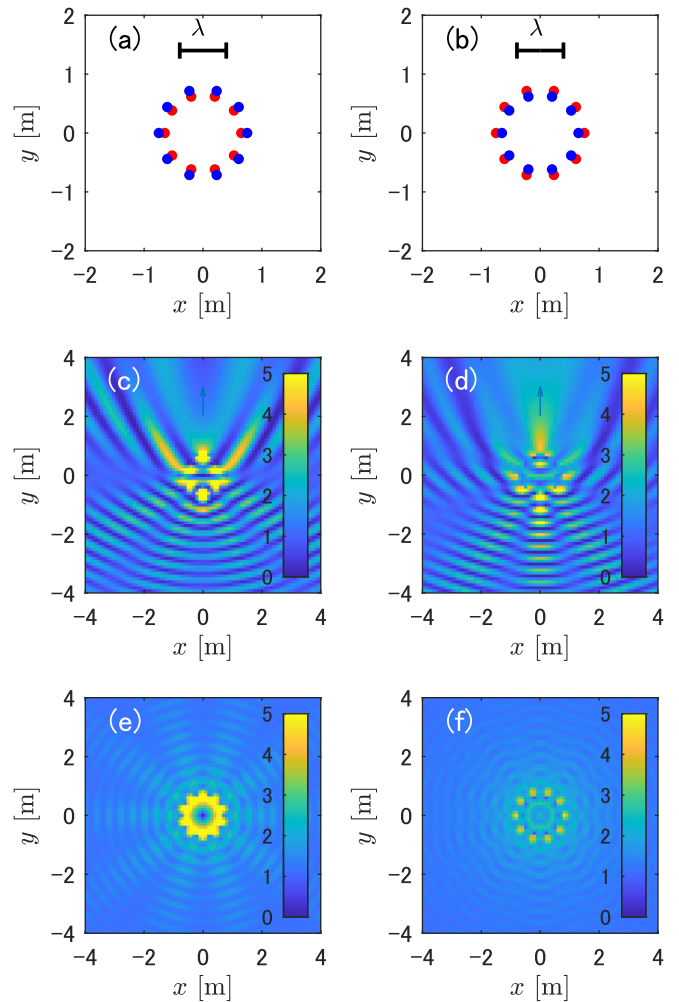

FIG. 6. Fields and field flows in an ensemble of HR dipoles. (a) and (b) Distributions of HRs in a 2D field, where in (a) the gain of the dipole is inside of the circle and in (b) the gain is outside. (c) and (d) The normalized intensity field with the interactions with HRs distributed as in (a) and (b), where the incident wave arrives from the bottom in the direction of the arrows at a frequency of $f = 430.5$ Hz. (e) and (f) Intensity fields averaged over the incident directions for every 5°. A comparison between (e) and (f) clearly shows the sound concentration effect of (e) when the gain is inside of the circle.

we also introduced a design method for the $\mathcal{PT}$-symmetric dipole using the Ewald limiting disk and 2D Fourier transform of analytically obtained $G(x, y)$ which proves the validity of the derived theoretical model by a comparison with numerical integration. The asymmetric scattering from such HR dipoles was demonstrated in a 2D experiment, where the non-Hermitian HR dipole was formed by a neutral HR and a HR with loss. We note that the experimental results and the predictions directly show good agreement without any fitting parameters. Finally, we showed how assemblies of such dipoles may be used to design a metastructure for the control of the sound flow. Indeed, a sound field concentration in the 2D field is predicted using a circular arrangement of $\mathcal{PT}$-symmetric HR dipoles. The study may provide a new platform for several applications to create nontrivial sound field propagation control on the basis of $\mathcal{PT}$ symmetry breaking.
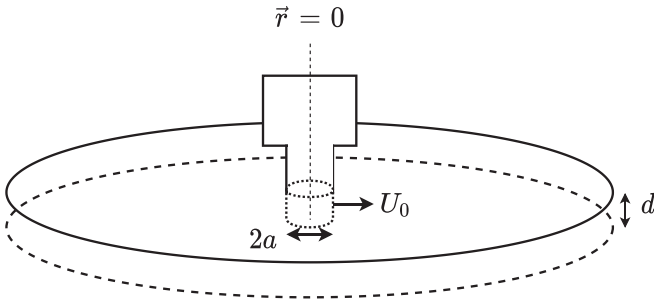
$$\vec{r} = 0$$

FIG. 7. HR in 2D space.

APPENDIX A: DERIVATION OF THE GAIN FUNCTION OF THE HELMHOLTZ RESONATOR IN 2D SPACE

We here analyze the response of a HR coupled to the planar waveguiding mode of the 2D space by deriving its gain function. The main geometrical features of the system are displayed in Fig. 7.

We first derive the relationship between the incident wave at the position of the HR ($\vec{r} = \vec{0}$) and the scattered wave in the arbitrary position $P_{\text{scat}}(\vec{r})$. The decay of the two-dimensional field can be expressed by the Hankel function:

$$P_{\text{scat}}(\vec{r}) = H_0^{(2)}(kr)P_{\text{out}}(\vec{0}). \tag{A1}$$

Generally, the scattered wave can be expressed through the incident wave $P_{\text{in}}(\vec{0})$, the zero-order Hankel function $H_0^{(2)}(kr)$, and the normalized gain $G(\omega) = P_{\text{out}}(\vec{0})/P_{\text{in}}(\vec{0})$:

$$P_{\text{scat}}(\vec{r}) = G(\omega)H_0^{(2)}(kr)P_{\text{in}}(\vec{0}). \tag{A2}$$

In terms of the particle velocity U_0 of the scattered wave at $r = a$ (a is the radius of the HR) the pressure of the wave at any arbitrary position can be expressed as follows [27]:

$$P_{\text{scat}}(\vec{r}) = \frac{i\omega\rho_0}{k}\frac{H_0^{(2)}(kr)}{H_1^{(2)}(ka)}U_0 e^{i\omega t}. \tag{A3}$$

In order to eliminate U_0 from Eq. (A3), we use the equivalence of the volume velocity at the cross section of the HR neck and at the side of the cylinder-shaped section which is illustrated by a dotted line with the same radius as the HR neck and placed below the HR. Such equivalence resumes in the following expression:

$$S_h\dot{\eta} = -2\pi a d U_0 e^{i\omega t}, \tag{A4}$$

where η denotes the displacement of the air inside the HR neck. Then we use the relation between displacement and pressure inside HR [28]:

$$P(\vec{0}) = \rho_0 l'\left(\omega_0^2 - \omega^2 + i\gamma\omega\right)\eta, \tag{A5}$$

where we have added a term of friction proportional to the particle velocity and $P(\vec{0})$ denotes the total pressure field

$P_{\text{in}}(\vec{0}) + P_{\text{scat}}(\vec{0})$. Substituting Eq. (A5) into Eq. (A4) leads to

$$U_0 e^{i\omega t} = -\frac{S_h}{2\pi a d}\frac{i\omega}{\rho_0 l'}\frac{P(\vec{0})}{\omega_0^2 - \omega^2 + i\gamma\omega}, \tag{A6}$$

where we assume that $P_{\text{scat}}(\vec{r})$ and $P_{\text{in}}(\vec{r})$ are constant when $r \leqslant a$:

$$P_{\text{scat}}(\vec{r}) = H_0^{(2)}(ka)P_{\text{out}}(\vec{0}), \tag{A7}$$

$$P_{\text{in}}(\vec{r}) = P_{\text{in}}(\vec{0}). \tag{A8}$$

The substitution of Eq. (A6) in Eq. (A3) gives

$$P_{\text{scat}}(\vec{r}) \approx H_0^{(2)}(kr)G_0(\omega)[P_{\text{in}}(\vec{0}) + P_{\text{scat}}(\vec{0})], \tag{A9}$$

where we use the approximation of the first-order Hankel function under the condition $ka \ll 1$:

$$H_1^{(2)}(ka) \approx i\frac{2}{\pi}\frac{1}{ka}. \tag{A10}$$

Finally, taking Eq. (A7) and substituting $\vec{r} = \vec{a}$ into Eq. (A9) lead to

$$P_{\text{out}}(\vec{0}) = G_0(\omega)[P_{\text{in}}(\vec{0}) + H_0^{(2)}(ka)P_{\text{out}}(\vec{0})], \tag{A11}$$

and the gain function $G(\omega) = P_{\text{out}}(\vec{0})/P_{\text{in}}(\vec{0})$ is therefore derived as

$$G(\omega) = \frac{1}{G_0^{-1}(\omega) - 1 - i\frac{2}{\pi}\ln\left(\frac{2}{\epsilon ka}\right)}, \tag{A12}$$

where, again, we use the approximation of the zero-order Hankel function under the condition $ka \ll 1$:

$$H_0^{(2)}(ka) \approx 1 + i\frac{2}{\pi}\ln\left(\frac{2}{\epsilon ka}\right). \tag{A13}$$

APPENDIX B: EWALD LIMITING DISK

The multistatic matrix in Fig. 3 allows us to recover the Ewald limiting disk (ELD) [29] of the dipole [see Figs. 8(a) and 8(b)]. Knowing how the wave at angle α_{in} scatters to α_{out} allows us to reconstruct the spatial component of the ELD with $\vec{q} = (\vec{k_{\text{out}}} - \vec{k_{\text{out}}})$, where $\vec{k_{\text{in}}}$ and $\vec{k_{\text{out}}}$ have the modulus of k and direction determined by α_{in} and α_{out}, respectively. Note that the radius of the disk is $2k$.

Figures 8(c) and 8(d) show the reconstructed ELD from the multistatic matrix of the analytical calculation for two different frequencies, 432 and 440Hz (insets show the ELD obtained with COMSOL simulation data), while Figs. 8(e) and 8(f) show the two-dimensional Fourier transform of the gain function $G(x, y)$ for the two frequencies corresponding to Figs. 8(c) and 8(d) (insets show the reconstructed ELD analyzed assuming the first Born approximation), where $G(-D, 0) = G_1$, $G(D, 0) = G_2$ and $G(x, y) = 0$ if $(x, y) \neq (\pm D, 0)$.

Figures 8(c) and 8(e) depict the result at a frequency of 432 Hz, while Figs. 8(d) and 8(f) are obtained at 440 Hz. The comparisons between Figs. 8(c) and 8(d) and both respective insets show good agreement. This proves the validity of the analytic derivation of the formula shown in Sec. II A. It may also be observed that, in turn, both Figs. 8(e) and 8(f) also match their insets completely, demonstrating that the first Born approximation of the scattered field is calculated

(a) Multistatic matrix

(b) Ewald limiting disk

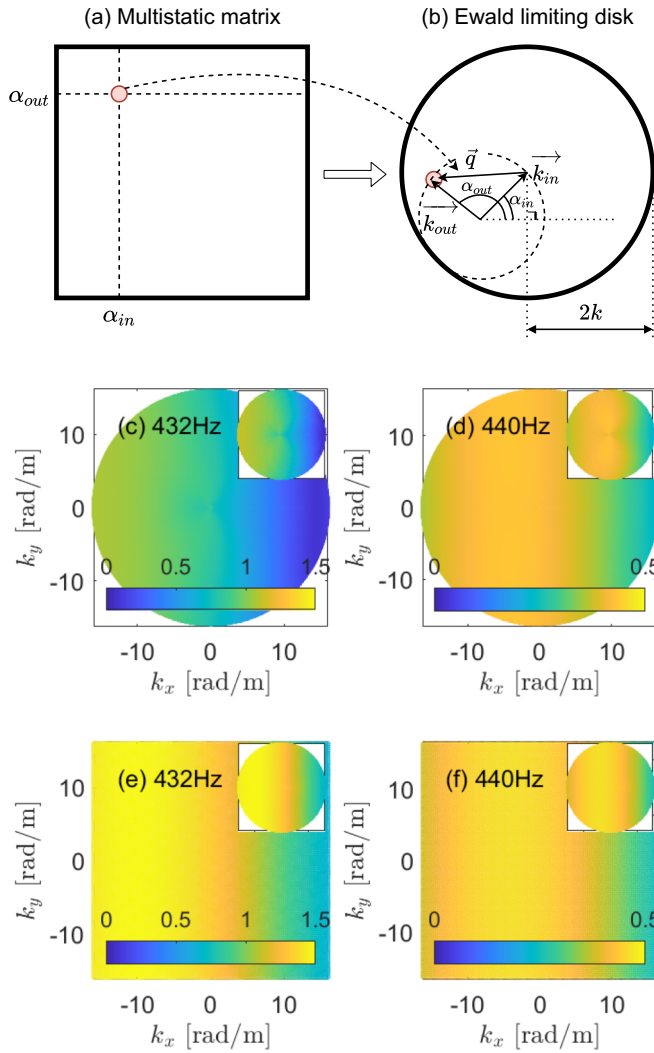(c) 432Hz

(d) 440Hz

(e) 432Hz

(f) 440Hz

FIG. 8. (a) The scheme of a multistatic matrix and (b) that of the Ewald limiting disk (ELD) reconstructed from (a) (Fig. 3). (c) The ELD reconstructed from Fig. 3(a) with a frequency of 432 Hz and (d) that for 440 Hz. (e) and (f) Spectrum distribution obtained directly from Fourier transform of the gain function. The insets of (c) and (d) show the ELD obtained by COMSOL simulation, while the insets of (e) and (f) show the reconstruction from a multistatic matrix analyzed with 1st Born approximation). (c) and (e) show the result for a frequency 432 Hz, and (d) and (f) show the result for 440 Hz.

from the 2D Fourier transform of the gain function $G(x, y)$. Furthermore, Figs. 8(d) and 8(f) show good agreement, including the insets, although the color at center of Fig. 8(d) is not vertically straight as in Fig. 8(f). In contrast, Figs. 8(c) and 8(e) are barely similar. The similarity come from the weakness of the interaction between HRs as expressed by the term $(\boldsymbol{I} - \boldsymbol{G H_0})^{-1}$ in Eq. (6). This fact suggests that one can design the $\mathcal{PT}$-symmetric dipole directly from the 2D Fourier transform of $G(x, y)$, at least when $(\boldsymbol{I} - \boldsymbol{G H_0})^{-1}$ is negligible.

Finally, Fig. 9 illustrates the relationship between the multistatic matrix and ELD to clarify the region in the ELD that needs to be differentiated in order to have a $\mathcal{PT}$ symmetry-breaking effect. Figure 9(a) is a multistatic matrix divided into four areas depending on whether the directions of the incident and scattered wave are right or left.

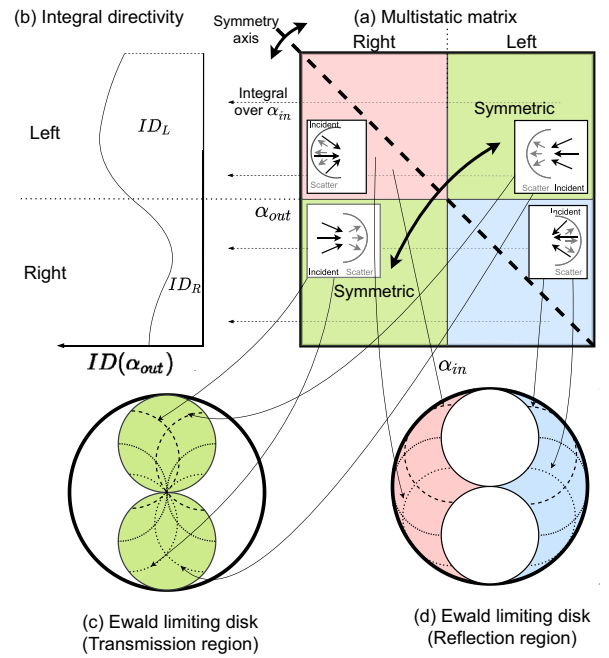(b) Integral directivity

(a) Multistatic matrix

FIG. 9. Relationship of ELD and transmission/reflection. (a) Multistatic matrix separated in four areas, where green areas are symmetric. The insets for each area show the directions of incident and scattered waves for each area, where the long black and short gray arrows denote incident and scattered waves, respectively. (b) Integral directivity plot calculated from the multistatic matrix by summing up the its values horizontally. It is obvious that the difference in ID_L and ID_R come from only blue and red areas in (a). (c) and (d) Two regions of ELD, where (c) illustrates the transmission region corresponding to green areas in (a) and (d) illustrates the reflection regions corresponding to blue and red areas.

The insets for each area show the directions of incident and scattered waves. The long and short arrows denote incident and scattered waves, respectively, and the half circle determines the scattering angular range for each area. As shown in Fig. 3, multistatic matrix has a diagonal symmetry axis, and the green areas in Fig. 9(a), which we call the transmission region, have the same components. In contrast, the blue and red areas, which we call the reflection region, may have different components. Figure 9(b) illustrates the ID plot calculated from Fig. 9(a). It is clear that the difference between $\mathrm{ID}_L(\alpha_{\mathrm{out}})$ and $\mathrm{ID}_R(\alpha_{\mathrm{out}})$ arises only from the blue and red areas in Fig. 9(a). Finally, Figs. 9(c) and 9(d) represent the two regions of the ELD, where Fig. 9(c) illustrates the transmission region, which corresponds to the green areas in Fig. 9(a), and Fig. 9(d) illustrates the reflection regions, which correspond to blue and red areas in Fig. 9(a). This implies that the asymmetric effects are accounted for by differences in the blue and red regions in Fig. 9(d). In fact, as we compare these regions in Figs. 8(c) and 8(d), it is obvious that the red region is much stronger than the blue one, which corresponds to the deflection shown in Fig. 4(a), where deflection to the left is observed at frequencies of 432 and 440 Hz. This tendency also holds for Figs. 8(e) and 8(f), suggesting that creating a strong contrast between these regions may be a guideline

when designing the $\mathcal{PT}$-symmetric dipole by a 2D Fourier transform of $G(x, y)$.

APPENDIX C: NON-HERMITIAN HR DIPOLE IN A 1D WAVEGUIDE

Here, we introduce the non-Hermitian HR dipole in a one-dimensional waveguide. When the incident wave is emitted from the left side (L) or from the right side (R), the reflection R_L and the transmission T can be described by the following formulas:

$$R_L = \left| \frac{G_1 e^{+2ikD} + G_2 e^{-2ikD} + 2G_1 G_2 e^{-4ikD}}{1 - G_1 G_2 e^{-4ikD}} \right|^2, \quad \text{(C1)}$$

$$T = \left| \frac{G_1 + G_2 + 2G_1 G_2 \cos 2kD}{1 - G_1 G_2 e^{-4ikD}} \right|^2, \quad \text{(C2)}$$

with

$$G_n(\omega) = \frac{1}{\gamma_{c1}^{-1}\left(\frac{\omega_0^2}{\omega} - \omega\right)i - \left(\frac{\gamma_n}{\gamma_{c1}} + 1\right)} \quad (n = 1, 2), \quad \text{(C3)}$$

$$\gamma_{c1} = \frac{cS_h}{2l'S}, \quad \text{(C4)}$$

where n stands for each HR and γ_{c1} is the coupling loss factor in one dimension; R_R is calculated using Eq. (C1) by exchanging the positions of the HRs, that is to say, by exchanging G_1 and G_2. The variables are commonly used in the 2D case in the main text, except the cross section of the 1D wave guide S. Note that, theoretically, there is no difference in the transmittance across systems in the direction of incidence.

We conducted an experiment to confirm the asymmetric response of the non-Hermitian dipole in a 1D case using the setup shown in Fig. 10(a). The values of the geometric parameters are the same as the ones used in the experiment conducted in two dimensions, described in Fig. 5, except $S = 1225$ mm^2. First, we measured the impulse responses (IRs) from the speaker to the microphones (MicRef, MicTrans), without attaching the HR dipole to the waveguide, to obtain the transfer functions (TFs) $P_{0,\text{Ref}}(\omega)$, $P_{0,\text{Trans}}(\omega)$. Next, we measured the IRs of each HR attached to the waveguide and obtained the TFs $P_{\text{Ref}}^{\text{HR}_1}(\omega)$, $P_{\text{Ref}}^{\text{HR}_2}(\omega)$ as well as the IRs of the dipole to get the TFs $P_{\text{Ref}}^{L}(\omega)$, $P_{\text{Trans}}^{L}(\omega)$. Finally, the gain functions and the reflectance and transmittance were calculated as

$$G_n(\omega) = \frac{P_{\text{Ref}}^{\text{HR}_n}(\omega) - P_{0,\text{Ref}}(\omega)}{P_{0,\text{Ref}}(\omega)}, \quad \text{(C5)}$$

$$R_L(\omega) = \left| \frac{P_{\text{Ref}}^{L}(\omega) - P_{0,\text{Ref}}(\omega)}{P_{0,\text{Ref}}(\omega)} \right|^2, \quad \text{(C6)}$$

$$T_L(\omega) = \left| \frac{P_{Trans}^{L}(\omega)}{P_{0,Trans}(\omega)} \right|^2. \quad \text{(C7)}$$

We provide comparisons of the experimental results and the theoretical calculation in Figs. 10(b)–10(e). Figures 10(b) and 10(c) show the experimental versus theoretical gain functions of both HRs, $G_1(\omega)$ and $G_2(\omega)$, while Figs. 10(d) and 10(e) illustrate experimental/theoretical frequency responses of the reflectances, R_L and R_R, and the transmittances, T_L and T_R. According to Figs. 10(b) and 10(c), HR1, having no loss, reaches 1 at the peak as expected, while HR2, with loss, has a
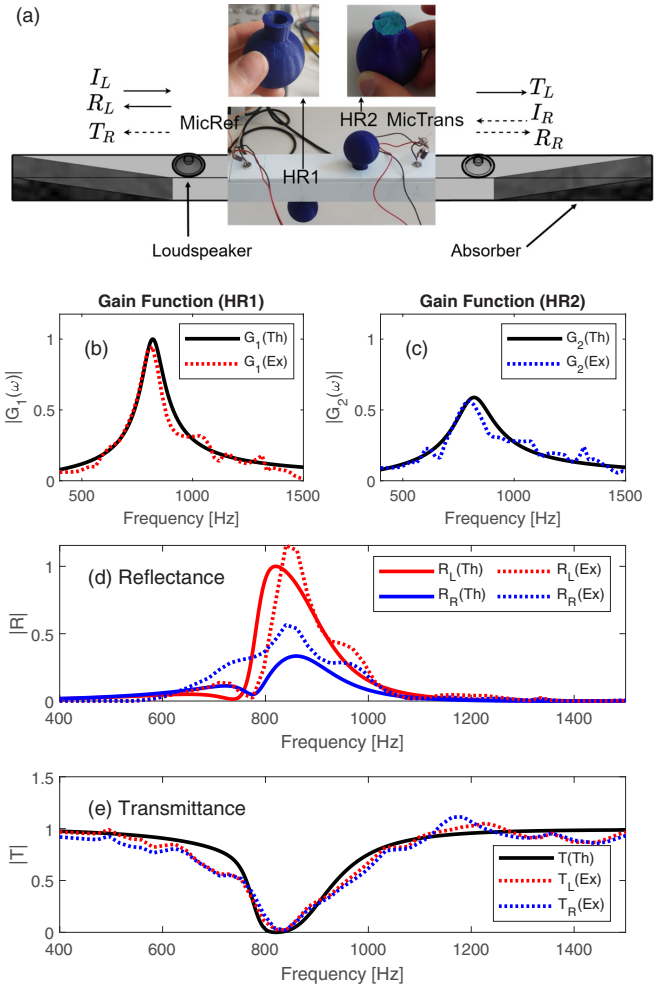

FIG. 10. Experimental setup and result of the 1D HR dipole. (a) Experimental setup for the HR dipole, composed of HR1 and HR2, in a 1D waveguide. Solid and dashed arrows denote the cases of initial sound incidence from the left and right, respectively. When the wave is incident from the right, MicRef and MicTrans exchange positions. (b) and (c) Frequency responses of gain functions for HR1 and HR2. Dashed and solid lines represent the experimental results and the theoretical calculations, where the parameters $f_0 = 820$ Hz, $\gamma_1/\gamma_{c1} = 0$, and $\gamma_2/\gamma_{c1} = 0.7$ were manually adjusted to fit the experimental results. (d) and (e) Frequency response of the reflectance and transmission of dipole. Red and blue lines denote the responses incident from the left and right, respectively. Dashed and the solid lines denote the experimental and theoretical results, respectively. Parameters adjusted in (b) and (c) were used for the theoretical calculations. The solid line in (e) is only colored black since the transmission is theoretically supposed to be the same for both incident directions.

peak smaller than unity. Using these responses of G_1 and G_2, we adjusted the parameters of the resonant frequency f_0 and the loss factor γ_n/γ_{c1}, as shown in Fig. 5. In Fig. 10(d), the significant asymmetry found in the reflectance was observed for both the theoretical calculation and the experimental measurements, resulting in good agreement, where we used the previously determined parameters f_0 and γ_n/γ_{c1} for the theoretical calculation. Furthermore, in Fig. 10(e), we can also observe good agreement for transmittance between experiment and the theory.

[1] C. M. Bender and S. Boettcher, Real Spectra in Non-Hermitian Hamiltonians Having $\mathcal{PT}$ Symmetry, Phys. Rev. Lett. **80**, 5243 (1998).

[2] S. A. R. Horsley, M. Artoni, and G. C. L. Rocca, Spatial Kramers–Kronig relations and the reflection of waves, Nat. Photonics **9**, 436 (2015).

[3] S. Longhi, Wave reflection in dielectric media obeying spatial Kramers-Kronig relations, Europhys. Lett. **112**, 64001 (2015).

[4] W. W. Ahmed, R. Herrero, M. Botey, and K. Staliunas, Locally parity-time-symmetric and globally parity-symmetric systems, Phys. Rev. A **94**, 053819 (2016).

[5] W. W. Ahmed, R. Herrero, M. Botey, Z. Hayran, H. Kurt, and K. Staliunas, Directionality fields generated by a local Hilbert transform, Phys. Rev. A **97**, 033824 (2018).

[6] Z. Hayran, H. Kurt, R. Herrero, M. Botey, K. Staliunas, and K. Staliunas, All-dielectric self-cloaked structures, ACS Photonics **5**, 2068 (2018).

[7] C. E. Rüter, K. G. Makris, R. El-Ganainy, D. N. Christodoulides, M. Segev, and D. Kip, Observation of parity–time symmetry in optics, Nat. Phys. **6**, 192 (2010).

[8] B. Peng, Ş. K. Özdemir, F. Lei, F. Monifi, M. Gianfreda, G. L. Long, S. Fan, F. Nori, C. M. Bender, and L. Yang, Parity–time-symmetric whispering-gallery microcavities, Nat. Phys. **10**, 394 (2014).

[9] K. G. Makris, R. El-Ganainy, D. N. Christodoulides, and Z. H. Musslimani, Beam Dynamics in $\mathcal{PT}$ Symmetric Optical Lattices, Phys. Rev. Lett. **100**, 103904 (2008).

[10] S. Longhi, Bloch Oscillations in Complex Crystals with $\mathcal{PT}$ Symmetry, Phys. Rev. Lett. **103**, 123601 (2009).

[11] S. A. R. Horsley, C. G. King, and T. G. Philbin, Wave propagation in complex coordinates, J. Opt. **18**, 044016 (2016).

[12] Z. Hayran, R. Herrero, M. Botey, H. Kurt, and K. Staliunas, Invisibility on demand based on a generalized Hilbert transform, Phys. Rev. A **98**, 013822 (2018).

[13] L. Feng, Y.-L. Xu, W. S. Fegadolli, M.-H. Lu, J. E. B. Oliveira, V. R. Almeida, Y.-F. Chen, and A. Scherer, Experimental demonstration of a unidirectional reflectionless parity-time metamaterial at optical frequencies, Nat. Mater. **12**, 108 (2012).

[14] A. Guo, G. J. Salamo, D. Duchesne, R. Morandotti, M. Volatier-Ravat, V. Aimez, G. A. Siviloglou, and D. N. Christodoulides, Observation of $\mathcal{PT}$-Symmetry Breaking in Complex Optical Potentials, Phys. Rev. Lett. **103**, 093902 (2009).

[15] J. Medina Pardell, R. Herrero, M. Botey, and K. Staliunas, Stabilized narrow-beam emission from broad-area semiconductor lasers, Phys. Rev. A **101**, 033833 (2020).

[16] Z. Lin, H. Ramezani, T. Eichelkraut, T. Kottos, H. Cao, and D. N. Christodoulides, Unidirectional Invisibility Induced by $\mathcal{PT}$-Symmetric Periodic Structures, Phys. Rev. Lett. **106**, 213901 (2011).

[17] Y. D. Chong, L. Ge, and A. D. Stone, $\mathcal{PT}$-Symmetry Breaking and Laser-Absorber Modes in Optical Scattering Systems, Phys. Rev. Lett. **106**, 093902 (2011).

[18] T. Chen, W. Tang, J. Mu, and T. J. Cui, Microwave metamaterials, Ann. Phys. (Berlin, Ger.) **531**, 1800445 (2019).

[19] S. Longhi, Half-spectral unidirectional invisibility in non-Hermitian periodic optical structures, Opt. Lett. **40**, 5694 (2015).

[20] H. Long, Y. Cheng, and X. Liu, Asymmetric absorber with multiband and broadband for low-frequency sound, Appl. Phys. Lett. **111**, 143502 (2017).

[21] I. Herrero-Durá, A. Cebrecos, R. Picó, V. Romero-García, L. M. García-Raffi, and V. J. Sánchez-Morcillo, Sound absorption and diffusion by 2D arrays of Helmholtz resonators, Appl. Sci. **10**, 1690 (2020).

[22] K. Staliunas, P. Markoš, and V. Kuzmiak, Scattering properties of a $\mathcal{PT}$ dipole, Phys. Rev. A **96**, 043852 (2017).

[23] M. M. Sadeghi, S. Li, L. Xu, B. Hou, and H. Chen, Transformation optics with Fabry-Pérot resonances, Sci. Rep. **5**, 8680 (2015).

[24] H. Chen, Y. Zhou, M. Zhou, L. Xu, and Q. H. Liu, Perfect Undetectable Acoustic Device from Fabry-Pérot Resonances, Phys. Rev. Appl. **9**, 024014 (2018).

[25] M. H. Fakheri, A. Abdolali, and H. B. Sedeh, Arbitrary Shaped Acoustic Concentrators Enabled by Null Media, Phys. Rev. Appl. **13**, 034004 (2020).

[26] *Acoustic Metamaterials*, edited by R. V. Craster and S. Guenneau (Springer, Dordrecht, 2013).

[27] E. Williams, *Fourier Acoustics: Sound Radiation and Nearfield Acoustical Holography* (Academic, San Diego, 1999).

[28] S. H. Lee and O. B. Wright, Origin of negative density and modulus in acoustic metamaterials, Phys. Rev. B **93**, 024302 (2016).

[29] M. Born, E. Wolf, A. B. Bhatia, P. C. Clemmow, D. Gabor, A. R. Stokes, A. M. Taylor, P. A. Wayman, and W. L. Wilcock, *Principles of Optics: Electromagnetic Theory of Propagation, Interference and Diffraction of Light*, 7th ed. (Cambridge University Press, Cambridge, 1999).